



Superfluid stiffness of a KTaO_3 -based two-dimensional electron gas

S Mallik, G C Ménard, G Saiz, H Witt, J Lesueur, Alexandre Gloter, L Benfatto, M Bibes, N Bergeal

► To cite this version:

S Mallik, G C Ménard, G Saiz, H Witt, J Lesueur, et al.. Superfluid stiffness of a KTaO_3 -based two-dimensional electron gas. Nature Communications, 2022, 13, 10.1038/s41467-022-32242-y . hal-03853152

HAL Id: hal-03853152

<https://hal.science/hal-03853152>

Submitted on 15 Nov 2022

HAL is a multi-disciplinary open access archive for the deposit and dissemination of scientific research documents, whether they are published or not. The documents may come from teaching and research institutions in France or abroad, or from public or private research centers.

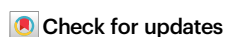
L'archive ouverte pluridisciplinaire **HAL**, est destinée au dépôt et à la diffusion de documents scientifiques de niveau recherche, publiés ou non, émanant des établissements d'enseignement et de recherche français ou étrangers, des laboratoires publics ou privés.

Superfluid stiffness of a KTaO_3 -based two-dimensional electron gas

Received: 18 February 2022

Accepted: 21 July 2022

Published online: 08 August 2022



S. Mallik^{1,5}, G. C. Ménard^{2,5}, G. Saiz^{2,5}, H. Witt^{1,2}, J. Lesueur², A. Gloter³,
L. Benfatto⁴, M. Bibes¹ & N. Bergeal² ✉

After almost twenty years of intense work on the celebrated $\text{LaAlO}_3/\text{SrTiO}_3$ -system, the recent discovery of a superconducting two-dimensional electron gas (2-DEG) in (111)-oriented KTaO_3 -based heterostructures injects new momentum to the field of oxides interface. However, while both interfaces share common properties, experiments also suggest important differences between the two systems. Here, we report gate tunable superconductivity in 2-DEGs generated at the surface of a (111)-oriented KTaO_3 crystal by the simple sputtering of a thin Al layer. We extract the superfluid stiffness of the 2-DEGs and show that its temperature dependence is consistent with a node-less superconducting order parameter having a gap value larger than expected within a simple BCS weak-coupling limit model. The superconducting transition follows the Berezinskii-Kosterlitz-Thouless scenario, which was not reported on SrTiO_3 -based interfaces. Our finding offers innovative perspectives for fundamental science but also for device applications in a variety of fields such as spin-orbitronics and topological electronics.

Potassium tantalate KTaO_3 is a band insulator with a 3.6 eV gap that retains a cubic perovskite structure down to the lowest temperature¹. Like strontium titanate (SrTiO_3), it is a quantum paraelectric material on the verge of a ferroelectric instability that is characterized by a large permittivity at low temperature ($\epsilon_r \approx 5000$)^{1,2}. Both materials can be turned into metal by electron doping, through oxygen vacancies, for example. Because of their common properties, it was suggested that superconductivity should also occur in doped KTaO_3 . However, while superconductivity was discovered more than half a century ago in bulk SrTiO_3 ³, all the attempts to induce bulk superconductivity in KTaO_3 -have failed so far⁴. Using ionic gating, Ueno et al. could generate a superconducting 2-DEG at the surface of (001)- KTaO_3 , albeit at a very low temperature ($T_c \approx 40$ mK)⁵. Later explorations of KTaO_3 2-DEGs did not evidence any superconductivity until the beginning of the year 2021, when two articles reported the discovery of superconducting 2-DEG formed at the interface between (111)- KTaO_3 and insulating overlayers of LaAlO_3 or EuO ^{6,7}. An empiric increase of T_c with electron

density was proposed with a maximum value of 2.2 K for doping of $\approx 1.04 \times 10^{14} \text{ e}^- \times \text{cm}^{-2}$ ⁶, which is almost one order of magnitude higher than in the $\text{LaAlO}_3/\text{SrTiO}_3$ interface⁸. An electric field effect control of the T_c was also demonstrated in a Hall bar device⁷ and a dome-shaped superconducting phase diagram similar to that of SrTiO_3 -based interfaces was derived^{9,10}. Following this discovery, the (110)-oriented KTaO_3 interface was also found to be superconducting with $T_c \approx 1$ K¹¹. It was recently proposed that the soft transverse optical mode, involved in the quantum paraelectricity, could be responsible for electron pairing in KTaO_3 interfaces. The coupling amplitude between this phonon mode and electrons is expected to be maximum in the (111) orientation and minimum in the (001) one, which would explain the hierarchy in T_c observed in these superconducting 2-DEGs¹².

In conventional superconductors, well described by the Bardeen–Cooper–Schrieffer (BCS) theory, the superconducting transition is controlled by the breaking of Cooper pairs as the temperature exceeds the energy scale set by the superconducting gap.

¹Unité Mixte de Physique, CNRS, Thales, Université Paris-Saclay, 1 Avenue Augustin Fresnel, 91767 Palaiseau, France. ²Laboratoire de Physique et d'Etude des Matériaux, ESPCI Paris, PSL University, CNRS, Sorbonne Université, Paris, France. ³Laboratoire de Physique des Solides, Université Paris-Saclay, CNRS UMR 8502, 91405 Orsay, France. ⁴Department of Physics and ISC-CNR, Sapienza University of Rome, Rome, Italy. ⁵These authors contributed equally: S. Mallik, G. Ménard, G. Saiz. ✉e-mail: nicolas.bergeal@espci.fr

However, in two-dimensional superconductors, the superfluid stiffness, i.e., the energy associated with the phase rigidity of the superconducting condensate, can be comparable to the pairing energy, allowing for a T_c suppression driven by the loss of phase coherence. In this case, the transition is expected to belong to the Berezinskii–Kosterlitz–Thouless (BKT) universality class, where the transition is controlled by the unbinding of topological vortex–antivortex pairs^{13–15}. Critical magnetic field measurements in (111)-KTO₃ 2-DEGs, both in the perpendicular and in the parallel geometry, set an upper bound, $d \approx 5$ nm, on the extension of the 2-DEG in the substrate⁶. This is lower than the superconducting coherence length, $\xi \approx 10$ – 15 nm⁶, which confirms that the superconducting 2-DEG is within the 2D limit. In addition, the presence of disorder, which has been identified in this system^{6,7}, is also expected to lower the superfluid rigidity and reinforce the role of phase fluctuations. Even though the measurements of the current–voltage characteristics in ref. 6 could be compatible with indirect signatures of a BKT transition, a direct measurement of the superfluid stiffness is required to properly address this issue¹⁶.

Here, we show that a 2-DEG can be generated at the surface of a (111)-oriented KTO₃ crystal simply by sputtering a very thin Al layer. The deposition of Al leads to the reduction of Ta ions as evidenced by X-ray photoelectron spectroscopy (XPS) and leads to the formation of an interfacial gate-tunable superconducting 2-DEG. We use resonant microwave transport to measure the complex conductivity of the 2-DEG and extract the temperature-dependent superfluid stiffness $J_s(T)$. Our results are consistent with a node-less superconducting order parameter in a rather strong-coupling regime ($\Delta(0)/k_B T_c^0 = 2.3$). Taking into account the presence of disorder and finite-frequency effect, we show that the superconducting transition follows the Berezinskii–Kosterlitz–Thouless model, which was not observed on SrTiO₃-based interfaces.

Results

2-DEGs were generated by dc sputtering of a very thin Al layer on (111)-oriented KTO₃ substrates at a temperature between 550 and 600 °C. The preparation process is detailed in the Methods section. Prior to deposition, we measured the in-situ X-ray photoelectron spectra (XPS) of the Ta 4f valence state (Fig. 1a top) of the KTO₃ substrate. The spectra show the sole presence of Ta⁵⁺ states (4f_{5/2} and 4f_{3/2}), indicating the expected stoichiometry of the substrate. The Ta 4f core levels were then measured after growing 1.8–1.9 nm of Al and transferring the sample in vacuum into the XPS setup. The bottom graph in Fig. 1a shows the Ta 4f core level spectra with additional peaks corresponding to reduced states of Ta i.e., Ta⁴⁺ and Ta²⁺. The deeper and lighter shades of same-colored peaks correspond to 4f_{5/2} and 4f_{3/2} split peaks. The reduction of Ta⁵⁺ to Ta⁴⁺ upon Al deposition indicates the formation of oxygen vacancies at the surface of KTO₃, which in turn suggests the formation of a 2-DEG. The Ta²⁺ signal may be due to the presence of a small amount of Ta in the AlO_x layer (akin to the situation in AlO_x/STO¹⁷) or reflects the presence of small clusters of oxygen vacancies around some Ta ions, reducing their apparent valence state. We monitored the Al oxidation state by measuring the Al 2p core levels after exposure of the sample to the atmosphere, which evidenced full oxidation of the Al layer into AlO_x. Thus, as in the AlO_x/SrTiO₃ system, the 2-DEG is formed through a redox process by which oxygens are transferred from the KTO₃ substrate to the Al overlayer^{17–19}.

The structure of the AlO_x/KTO₃ (111) interface has been imaged by scanning transmission electron microscopy (STEM). Figure 1b depicts the high-angle annular dark field (HAADF) - STEM image in cross-section. The electron energy loss spectroscopy (EELS) indicates that a small amount of K and Ta diffuse into the AlO_x layer. In contrast, the Al signal decays very rapidly in KTO₃, indicating no Al diffusion into KTO₃. Our fabrication method based on the sputtering of a thin Al film has already been successfully implemented to generate 2-DEGs

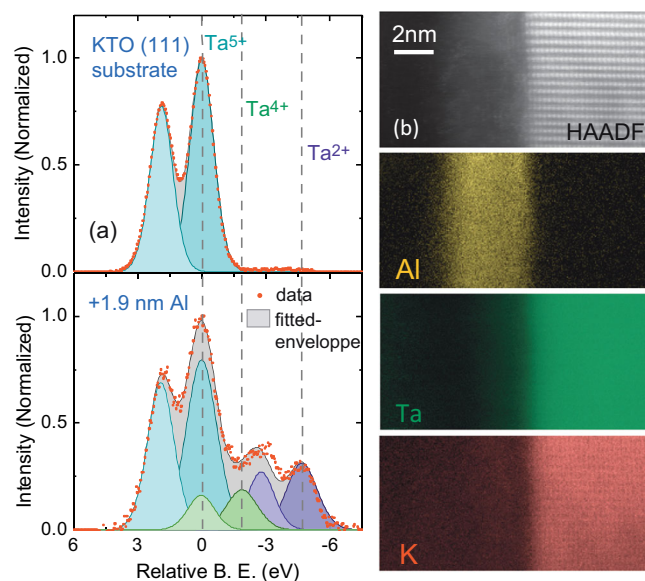


Fig. 1 | XPS and STEM characterization of the AlO_x/KTO₃ samples. **a** X-ray photoelectron spectra near the 4f core level binding energy of Ta for a KTO₃ substrate prior to deposition (top) and after deposition of 1.8 nm of Al (bottom). The fitted peaks for Ta⁵⁺, Ta⁴⁺, and Ta²⁺ are shown in cyan, green and violet colors, respectively. The deeper and lighter shades of the same colors represent the 4f_{5/2} and 4f_{3/2} valence states of the respective peaks. The data and sum fit envelope are shown in red circles and black lines. **b** (top) HAADF scanning transmission electron microscopy image at the cross-section of KTO₃ (111) and AlO_x interface. The KTO₃ is observed along the [112] direction. (down) EELS maps (Al-L_{2,3}, Ta-O_{2,3}, and K-L_{2,3} edges) showing the presence of Al on top of the interface without any interdiffusion but with some limited diffusion of Ta and K inside the AlO_x layer.

on (001)-oriented KTO₃ substrates showing a fivefold enhancement of the Rashba spin–orbit coupling as compared to SrTiO₃²⁰. In the present work, four samples, labeled A, B, C, and D, have been investigated by transport measurement at low temperature in a dilution refrigerator (see Methods section for fabrication parameters).

Figure 2a shows the resistance vs temperature curve of sample A on a wide temperature range revealing a superconducting transition at $T_c \approx 0.9$ K. In Fig. 2b, we plot the T_c as a function of the 2D carrier density, n_{2D} for the different samples studied and compare their values with those extracted from ref. 6. Our results confirm the trend observed in the literature (T_c increases with the carrier density) and demonstrate that our growth method, while being much easier to implement than the molecular beam epitaxy of a rare-earth element such as Eu or the pulsed laser deposition of a complex oxide, is able to produce good quality samples with similar T_c . The resistance vs temperature curves of sample B measured for different values of a magnetic field applied perpendicularly to the sample plane are shown in Fig. 2c. The temperature dependence of the critical magnetic field is consistent with a Landau–Ginsburg model near T_c , $\mu_0 H_c(T) = \frac{\Phi_0}{2\pi\xi^2(T)}$, taking into account an in-plane superconducting coherence length $\xi_{||} = \xi_{||}(0)(1 - \frac{T}{T_c})^{-1/2}$. We found $\xi_{||}(T=0) \approx 27$ nm, which is comparable with the value reported in ref. 6.

Although KTO₃ is a quantum paraelectric material like SrTiO₃, its permittivity is reduced by a factor of five as compared to SrTiO₃, making the electric field effect less efficient in a back-gating configuration¹². To overcome this difficulty, we prepared an AlO_x/KTO₃ sample using a thinner substrate (150 μm). After cooling the sample, the back-gate voltage was first swept to its maximum value $V_G = 200$ V while keeping the 2-DEG at the electrical ground. This forming procedure is commonly applied on SrTiO₃-based interfaces to ensure the reversibility of the gate sweeps in further gating sequences²¹. Figure 3 shows the sheet resistance of sample C as a

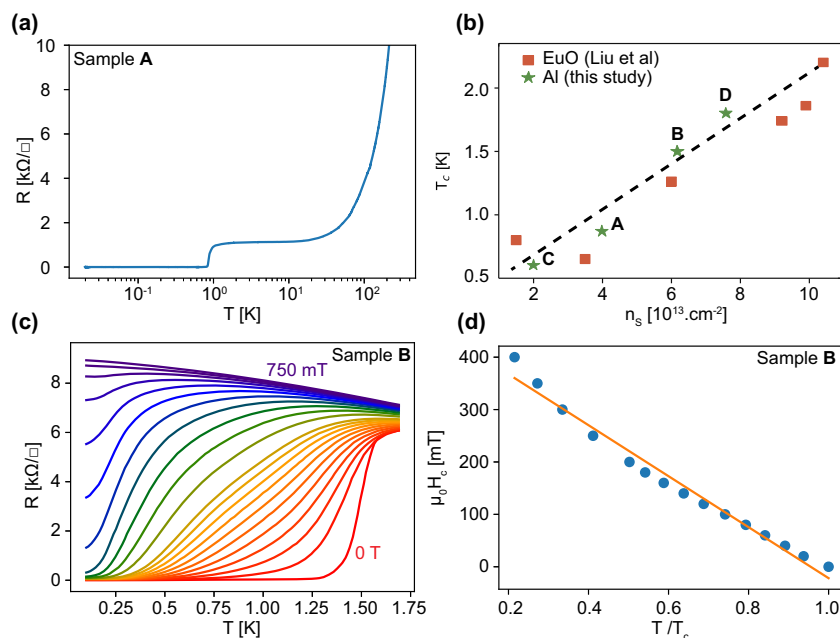


Fig. 2 | Magneto-transport characterization. **a** Sheet resistance of sample A as a function of temperature (log scale) showing a superconducting transition at $T_c \approx 0.9$ K. **b** Summary of the superconducting critical temperature as a function of the carrier density for all samples studied in this work compared with results from

ref. 6. **c** Sheet resistivity of sample B as a function of temperature for increasing magnetic fields between 0 and 750 mT. **d** Perpendicular critical magnetic field defined by a 50% drop of the normal-state resistance measured at $T = 1.65$ K. The orange line corresponds to a linear fit with the Ginsburg Landau formula.

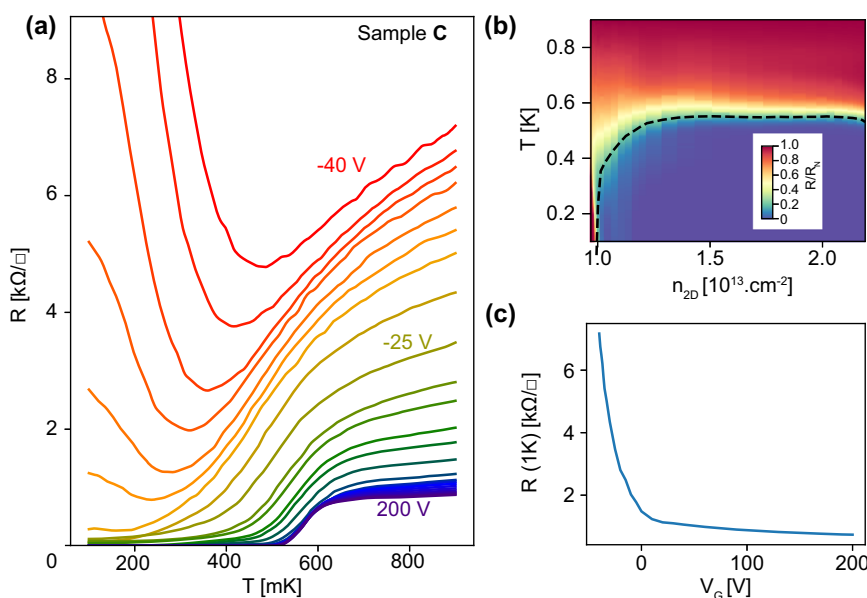


Fig. 3 | Electric field effect and superconducting phase diagram. **a** Temperature dependence of the sheet resistance of sample C for different values of the back-gate voltage in the range -40 to 200 V. **b** Normalized sheet resistance in color scale as a function of the carrier density extracted from Hall measurements and temperature.

The dashed line indicates the critical temperature defined by an 80% drop of the resistance with respect to the normal resistance R_N at $T = 0.9$ K. **c** Sheet resistance at 0.9 K as a function of the back-gate voltage.

function of temperature for different values of the gate voltage between -40 and 200 V. Electrostatic gating induces both a modulation of the normal-state resistance and a variation of the superconducting critical temperature. For negative gate voltages corresponding to a depleted quantum well, R vs T curves exhibit a quasi-reentrant behavior: the resistance first decreases and then upturns upon further cooling^{22,23}. This is characteristic of disordered superconducting thin films in which superconductivity only exists locally, forming a network of isolated islands surrounded by an

insulating medium that precludes percolation. While the decrease of resistance marks the emergence of superconductivity inside the islands, the upturn of resistance at low-temperature results from the opening of a gap in the excitation spectrum, which prevents the flow of quasiparticles across islands. Hence, the resistance does not reach zero, indicating that the superconducting order does not extend at a long range. As carriers are added upon increasing the gate voltage, the resistance curves flatten at low temperature, and the 2-DEG eventually reaches a true zero resistive state ($V_G > -25$ V). Long-range

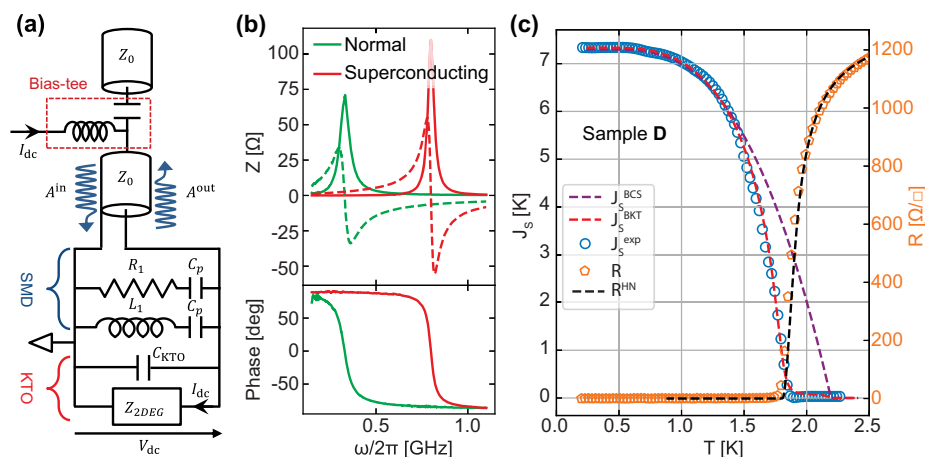


Fig. 4 | Microwave measurement of the KTaO₃ 2-DEG. **a** Schematics of the measurement setup adapted from ref. 26. The contribution of the sample is represented by the 2-DEG impedance, Z_{2DEG} , and the parallel capacitive contribution of the KTaO₃ substrate, C_{KTO} . SMD components, resistor $R_1 = 75 \Omega$, inductor $L_1 = 6.5 \text{ nH}$, are placed in parallel to define a resonating circuit. Large SMD capacitors $C_p = 2 \mu\text{F}$ block the dc signals in L_1 and R_1 without influencing the signals at microwave frequencies. The reflection coefficient at the circuit sample $\Gamma(\omega) = \frac{A^{\text{out}}}{A^{\text{in}}}$ is extracted from the measurement as described in ref. 26. A bias-tee is used to separate the dc current and the microwave one. **b** Top: Real (full lines) and imaginary (dashed lines) parts of the 2-DEG impedance as a function of frequency in the normal state at $T = 2.5 \text{ K}$ and in the superconducting state at $T = 0.2 \text{ K}$ after a

calibration procedure²⁶. Bottom: corresponding phases of the 2-DEG impedance in the normal and superconducting state. The resonance frequency of the sample circuit can be clearly identified, for instance, as the maximum of the peak in the real part of the impedance or as a π phase shift in its phase. **c** Superfluid stiffness J_s^{exp} extracted from the resonance frequency and Eq. (1) as a function of the temperature. The dashed purple line shows an attempt to fit the experimental data within a standard BCS model (J_s^{BCS}), which provides a mean field $T_c^0 = 2.3 \text{ K}$. A better agreement is obtained by using a BKT model (J_s^{BKT}). On the right axis, the figure also shows the sheet resistance curve (R) fitted with the Halperin and Nelson formula (R_{HN}).

superconducting order is established through Josephson coupling between the islands. Further doping makes the network of islands denser and increases the coupling between islands resulting in a “homogeneous-like” superconducting 2-DEG at high doping. The resulting superconducting phase diagram is shown in Fig. 3b, where the resistance is plotted in color scale as a function of temperature and electron density extracted by combining the Hall effect and gate capacitance measurements^{10,24}. In this experiment, the carrier density was tuned from $n_{2D} \approx 0.95 \times 10^{13} \text{ e}^- \times \text{cm}^{-2}$ to $n_{2D} \approx 2.2 \times 10^{13} \text{ e}^- \times \text{cm}^{-2}$, which is not sufficient to explain the modulation of the normal resistance by more than one order of magnitude. This indicates that the gate voltage not only controls the carrier density but also modifies deeply the electronic properties of the 2-DEG, in particular the electronic mobility, in agreement with the previous reports⁷.

We further investigated the superconducting KTaO₃ 2-DEG by measuring its superfluid stiffness J_s , which is the energy scale associated with the phase rigidity of the superconducting condensate. J_s is related to the imaginary part of the complex conductivity $\sigma(\omega) = \sigma_1(\omega) - i\sigma_2(\omega)$ of the superconductor that accounts for the transport of Cooper pairs at finite-frequency ω . This is a direct probe of the superconducting order parameter that provides important information on the nature of the superconducting state. In the low-frequency limit, $\hbar\omega \ll \Delta$, a superconductor displays an inductive response to an ac electrical current and $\sigma_2(\omega) = \frac{1}{L_k\omega}$, where L_k is the kinetic inductance of the superconductor that diverges at T_c ²⁵. The superfluid stiffness is then directly related to L_k

$$J_s(T) = \frac{\hbar^2}{4e^2 L_k(T)} \quad (1)$$

where \hbar is the reduced Planck constant and e is the electron charge.

We used resonant microwave transport to extract L_k below T_c and determine the superfluid stiffness of sample D as a function of temperature. The method, which was successfully applied to superconducting SrTiO₃-based interfaces, is illustrated in Fig. 4a and described in detail in refs. 26,27. In short, the KTaO₃ sample is embedded into a parallel RLC resonant electrical circuit made with

surface mount microwave devices (SMD). The capacitance of the circuit is dominated by the KTaO₃ substrate contribution (C_{KTO}) due to its large intrinsic permittivity. The total inductance of the circuit, $L_{\text{tot}}(T) = \frac{L_1 L_k(T)}{L_1 + L_k(T)}$, includes the contribution of an SMD inductor (L_1) and the contribution of the kinetic inductance L_k of the superconducting 2-DEG below T_c . Finally, an SMD resistor R_1 imposes that the dissipative part of the circuit impedance remains close to 50Ω in the entire temperature range, ensuring a good impedance matching with the microwave circuitry. The circuit resonates at the frequency $\omega_0 = \frac{1}{\sqrt{L_{\text{tot}} C_{KTO}}}$, which is accessed by measuring the reflection coefficient of the sample circuit $\Gamma(\omega) = \frac{A^{\text{out}}}{A^{\text{in}}} = \frac{Z(\omega) - Z_0}{Z(\omega) + Z_0}$. The resonance manifests itself as a peak in the real part of the circuit impedance, $Z(\omega)$, accompanied by a π phase shift²⁶. The height and the width of the peak are controlled by the dissipative part of the circuit impedance. In the superconducting state, the 2-DEG conductance acquires a kinetic inductance L_k that generates a shift of ω_0 towards high frequencies with respect to the normal state (Fig. 4b). The temperature-dependent superfluid stiffness J_s^{exp} , extracted from the resonance shift and Eq. (1) is presented in Fig. 4c (blue circles).

Discussion

The flattening of the J_s^{exp} curve below 1 K supports a fully gapped behavior, i.e., an absence of nodes in the order parameter. The purple dashed line (J_s^{BCS}) shows an attempt to fit the experimental curve with a standard BCS expression $J_s^{\text{BCS}}(T)/J_s(0) = (\Delta(T)/\Delta(0)) \tanh(\Delta(T)/k_B T)$ ²⁵, where $\Delta(T)$ is the superconducting gap obtained numerically by a self-consistent solution of the BCS equation, so that it vanishes at the mean-field temperature T_c^0 (i.e., the temperature at which Cooper pairs form). Since $J_s(0)$ is fixed by the experimental value at the lowest temperature, the only free parameter is then the ratio $\Delta(T=0)/k_B T_c^0$, that determines the curvature of the $J_s(T)$ curve. As one can see, even using a relatively strong-coupling value $\Delta(0)/k_B T_c^0 = 2.3$, from the fit of the low-temperature curve, one obtains $T_c^0 \approx 2.2 \text{ K}$, that is larger than the experimental T_c . To fit the data in the whole temperature range with the BCS expression only, one would then need an unreasonably large value ($\Delta(0)/k_B T_c^0 \approx 6$), a result that we checked to hold irrespectively of the exact functional BCS form used to fit the stiffness.

Here we follow a different approach and interpret the rapid drop of $J_s(T)$ below the BCS fit as a BKT signature, as we will discuss below. This interpretation is supported by a second striking observation that holds regardless of any specific consideration about its temperature dependence: the $T=0$ value of the stiffness $J_s(T=0) \approx 7.3$ K is of the same order as $T_c \approx 2.2$ K. It is worth noting that in conventional superconductors, where the superfluid density $n_s(T=0)$ is close to the carrier density n_{2D} , the stiffness at zero temperature is of the order of the Fermi energy, and then several orders of magnitude larger than T_c^0 . A strong reduction of $J_s(0)$ is instead observed in 2D-superconductors, where disorder strongly reduces n_s with respect to n_{2D} already at $T=0$ ^{28–38}. In the dirty limit, in which the elastic scattering rate $1/\tau$ is much larger than the superconducting gap, only a fraction of carriers, $n_s/n_{2D} \approx 2\Delta(0)/(\hbar/\tau)$, forms the superconducting condensate. In a single-band picture, an estimate of the superfluid stiffness is obtained from $\Delta(0)$ and the normal resistance R_N , $J_s \approx \frac{\pi\hbar\Delta(0)}{4e^2R_N}$. Using the previously estimated value of $\Delta(0) \approx 5$ K and $R_N \approx 1300 \Omega$, we obtain $J_s \approx 11.8$ K, close to the measured value ($J_s^{\text{exp}}(T=0) \approx 7.3$ K), which is consistent with the dirty limit.

The superfluid density of the 2-DEG can be directly deduced from the stiffness through the formula $n_s = \frac{4m}{\hbar^2} J_s$, where m is the effective mass of superconducting electrons. In the case of (111)-K₂FeO₄ 2-DEGs, the conduction band is derived from the bulk $J = 3/2$ states with a Fermi Surface formed by a hexagonal contour inside a sixfold symmetric star-shaped contour^{39,40}. Considering an average effective mass $m \approx 0.5m_0$, the corresponding superfluid density n_s extracted from J_s^{exp} is $n_s \approx 1.8 \times 10^{12} \text{ e}^- \text{ cm}^{-2}$, which is about 2.5% of the total carrier density ($n_{2D} = 7.5 \times 10^{13} \text{ e}^- \text{ cm}^{-2}$ for sample D). This very low ratio is comparable with previous findings in LaAlO₃/SrTiO₃ interfaces^{26,41,42}. Although such reduced superfluid density is consistent with the dirty limit, K₂FeO₄-(111) 2-DEG is a multiband system⁴⁰, in which superconductivity may involve only specific bands, as also suggested in SrTiO₃²⁶.

The reduced dimensionality and the suppression of the energy scale associated with the stiffness represent the prerequisites to observe BKT^{13–15} physics, since it makes the BKT temperature scale T_{BKT} associated with the unbinding of vortex-antivortex pairs far enough from T_c^0 ⁴³. The most famous hallmark of the BKT transitions is the discontinuous jump to zero of J_s at $T_{\text{BKT}} < T_c$ with a universal ratio $J_s(T_{\text{BKT}})/T_{\text{BKT}} = 2/\pi$ ⁴⁴. Such a prediction, theoretically based on the study of the 2D XY model^{13–15}, has been successfully confirmed in superfluid He films⁴⁵. In practice, the experimental observation of the BKT transition in real superconductors is more subtle. Indeed, in thin films, the suppression of n_s (and then J_s) with disorder comes along with an increasing inhomogeneity of the SC background, that is predicted to smear out the discontinuous superfluid-density jump^{35,46–48} into a rapid downturn, as observed experimentally via the direct measurement of the inverse penetration depth^{31–38} or indirectly via the measurement of the exponent of the nonlinear IV characteristics near T_c ^{16,28–30}. In the case of SrTiO₃-based interfaces, the direct measurement of J_s is rather challenging, and the few experimental reports available so far do not evidence a BKT jump^{26,41,42}.

Within the BKT approach, the effect of vortex-like topological excitations provides additional suppression of J_s with respect to the BCS dependence discussed above, driven only by quasiparticle excitations. To provide a fit of J_s^{exp} , we then solved numerically the renormalization-group (RG) equations of the BKT theory for the superfluid stiffness and vortex fugacity. As input parameters of the RG equations, we used the BCS temperature dependence of the stiffness. As mentioned above, the low-temperature part is fully captured by the BCS approximation, and for the estimated $\Delta(0)/k_B T_c^0$ ratio, the dirty-limit and the clean-limit expressions of J_s^{BCS} provide the same result. We also included the finite-frequency effects in our calculation^{43,49,50}. Indeed, even though the resonance frequency (about 0.5 GHz) is still small as compared to the optical gap (2Δ - 10 K - 200 GHz) it can nonetheless lead to non-negligible effects, in particular a rounding of

the jump and suppression of the stiffness at a temperature slightly larger than the one where the dc resistivity vanishes^{32,33,38}, as indeed observed in our case. The resistivity itself is consistently fitted with the interpolating Halperin–Nelson formula⁵⁰, which accounts for BKT-like fluctuations between T_{BKT} and T_c^0 , and for standard Gaussian fluctuations above T_c^0 . Finally, to account for spatial inhomogeneities, we introduce a gaussian distribution of local T_c and J_s with variance σ_G centered around T_c^0 and $J_s^{\text{exp}}(0)$. As seen in Fig. 4c, the result of the fitting procedure (dashed red line) is in very good agreement with experimental data both for the superfluid stiffness and the resistance, considering a very small inhomogeneity, $\sigma_G = 0.02$. Details on the fitting procedure are given in the Method Section.

Although K₂FeO₄ and SrTiO₃ have many common properties, the superconducting phases of their interfacial 2-DEG exhibit noticeable differences. Whereas a pure BCS weak-coupling limit with $\Delta(0)/k_B T_c \approx 1.76$ provides a very good description of superconductivity in SrTiO₃-based interfaces^{26,27}, we found a stronger value of the coupling for K₂FeO₄ ($\Delta(0)/k_B T_c \approx 2.3$). Such an important difference, which must be traced back to the pairing mechanism, is a strong constraint on the possible origin of superconductivity in these two materials. In addition, BKT physics was not observable in SrTiO₃ for which a simple BCS model without phase fluctuations was sufficient to fit the $J_s(T)$ curves with a very good accuracy²⁷. This may suggest more bosonic-like superconductivity in K₂FeO₄-based interfaces (in the highly doped regime), as evidenced by the large separation between the pairing scale, set by Δ , and the phase-coherence scale, set by the small value of the superfluid stiffness. Recent measurements of the in-plane critical field in K₂FeO₄-based interfaces suggested that the order parameter could be a mixture of s-wave and p-wave pairing components induced by strong spin-orbit coupling³¹. While we can not rule out this possibility, the saturation of the $J_s(T)$ curve below $T_c/2$ seen in Fig. 4b suggests a dominance of the fully gapped s-wave component. In addition, despite the complex band structure of the K₂FeO₄-(111) interfaces, we have not observed any signatures suggesting multi-gap superconductivity in our data. Further experiments, including tunneling spectroscopy, are therefore necessary to understand the nature of superconductivity in K₂FeO₄-based interfaces.

Methods

Sample fabrication

Prior to deposition, K₂FeO₄ (111) substrates from MTI corporation were annealed at 600 °C for 1 h in vacuum. Then, the thin Al layer was deposited in a dc magnetron sputtering system (PLASSYS MP450S) under a base pressure of the vacuum chamber lower than 5×10^{-8} mbar. During Al deposition, the Ar partial pressure and the dc power were kept fixed at 5×10^{-4} mbar and 10 W, respectively. The deposition rate for Al was 0.66 Å/s. Table 1 below summarizes the deposition parameters for the different samples.

XPS analysis

X-ray photoelectron spectroscopy (XPS) was measured using a non-monochromatized Mg K α source ($h\nu = 1253.6$ eV) in an Omicron NanoTechnology GmbH system with a base pressure of 5×10^{-10} mbar. The operating current and voltage of the source was 20 mA and 15 kV, respectively. Spectral analysis to determine different valence states of Ta were carried out using the CasaXPS software. Adventitious carbon was used as a charge reference to obtain the Ta 4f_{5/2} peak position for the fitting. The energy difference and the ratio of the area between 4f_{5/2} and 4f_{3/2} peaks for all the Ta valence states were constrained according to the previously reported values.

STEM characterization

STEM-HAADF and STEM-EELS measurements have been done at 100 keV using a Cs corrected Nikon STEM microscope and a Gatan modified EELS spectrometer equipped with a MerlinEM detector.

Table 1 | Growth parameters of the different samples used in this study

Samples	Deposition temp.	Al thickness	KTaO ₃ thickness
A	600 °C	1.8 nm	0.5 mm
B	500 °C	1.8 nm	0.5 mm
C	600 °C	1.8 nm	0.15 mm
D	500 °C first step RT second step	0.8 + 1.1 nm	0.5 mm

Theoretical analysis of $J_s(T)$

In order to account for vortex excitations, we solved the BKT RG equations^{15,43,44} for the vortex fugacity $g = 2\pi e^{-\mu/(k_B T)}$, with μ the vortex-core energy, and the rescaled stiffness $K \equiv \pi J_s/k_B T$:

$$\frac{dK}{d\ell} = -K^2 g^2, \quad (2)$$

$$\frac{dg}{d\ell} = (2 - K)g, \quad (3)$$

where $\ell = \ln(a/\xi_0)$ is the RG-scaled lattice spacing with respect to the coherence length ξ_0 , that controls the vortex sizes and appears as a short-scale cut-off for the theory. The initial values at $\ell = 0$ are set by the BCS fitting $J_s^{\text{BCS}}(T)$ of J_s^{exp} , and the renormalized stiffness is given by the large-scale behavior, $J_s = (k_B T/\pi)K(\ell \rightarrow \infty)$. The ratio $\mu/J_s = 0.87$, similar to the one found in other conventional superconductors^{34,35,37,38}, is used as a free (temperature-independent) parameter, which controls the strength of stiffness renormalization due to bound vortices below T_{BKT} ⁴³. To account for finite-frequency effects, we further include a dynamical screening of vortices^{49,50} via an effective frequency-dependence dielectric function $\varepsilon(\omega)$ which enters in the complex conductivity of the film as $\sigma(\omega) = -\frac{4J_s^{\text{BCS}} e^2}{i\omega \hbar^2 \varepsilon(\omega)}$. At zero frequency $\varepsilon(\omega)$ is real and $\varepsilon_1(0) = K(0)/K(\ell \rightarrow \infty) = J_s^{\text{BCS}}/J_s$ so one recovers the usual static result. At finite-frequency $\varepsilon(\omega)$ develops an imaginary part due to the vortex motion, that can be expressed in the first approximation⁴⁹ as $\varepsilon_2 \simeq (r_\omega/\xi)^2$, where ξ is the vortex correlation length and r_ω is a finite length scale set in by the finite frequency of the probe, i.e. $r_\omega = \sqrt{\frac{14D_v}{\omega}}$, with D_v the vortex diffusion constant of the vortices. The main effect of ε_2 is to induce a small tail above T_{BKT} for the finite-frequency stiffness, as given by $J_s = \hbar^2 \omega \sigma_2(\omega)/(4e^2)$, as we indeed observe in the experiments. Here we follow the same procedure outlined in ref. 38 to compute $\varepsilon(\omega)$, and in full analogy, with this previous work, we find a very small vortex diffusion constant $D_v \sim 10^{10} \text{ nm}^2/\text{s}$. The correlation length $\xi(T)$ also enters the temperature dependence of the resistivity above T_{BKT} , that follows the usual scaling $R/R_N = 1/\xi^2(T)$. To interpolate between the BKT and Gaussian regime of fluctuations, we use the well-known Halperin–Nelson expression^{43,46,50} $\xi_{\text{HN}}(T) = \frac{2}{A} \sinh\left(\frac{b}{\sqrt{t}}\right)$ where $t = (T - T_{\text{BKT}})/T_{\text{BKT}}$, and we set $A = 2.5$ and $b = 0.27$, consistent with the theoretical estimate of $b \simeq 0.2$ that we obtain from the value of μ ^{35,38,43}. Finally, to account for the possible inhomogeneity of the sample, we consider the extension of the previous method to the case where the overall complex conductivity of the sample is computed in the self-consistent effective-medium approximation⁵² as the solution of the following equation:

$$\sum_i P_i \frac{\sigma_i(\omega) - \sigma(\omega)}{\sigma_i(\omega) + \sigma(\omega)}. \quad (4)$$

Here $\sigma_i(\omega)$ denotes the complex conductivity of a local superconducting puddle with stiffness J_i and local T_c^i , that are taken with a Gaussian distribution P_i with variance σ_G centered around the BCS fit of J_s^{exp} . For each realization J_i we then compute the $J_{s,i}$ from the solution of the BKT equations (2)–(3), we determine the corresponding complex conductivity $\sigma_i(\omega)$ and we finally solve Eq. (4) to get the average

$J_s^{\text{BKT}} = (\hbar^2/4e^2)\omega\sigma_2(\omega)$ below T_c and the average $\sigma_1(\omega = 0) \equiv 1/R^{\text{HN}}$ above T_c , i.e., the dashed lines reported in Fig. 4c. Further details about the implementation of the effective-medium approximation can be found in refs. 16,38. The main effect of inhomogeneity is to contribute slightly to the suppression of J_s with respect to J_s^{BCS} before T_{BKT} . In our case, we checked that inhomogeneity, if present, is very small, and a $\sigma_G = 0.02$ is enough to account for the measured temperature dependences.

Data availability

The authors declare that the data that support the findings of this study are available within the article. All other relevant data are available from the corresponding authors upon request.

References

- Fujii, Y. & Sakudo, T. Dielectric and optical properties of KTaO₃. *J. Phys. Soc. Jpn.* **41**, 888–893 (1976).
- Fleury, P. A. & Worlock, J. M. Electric-field-induced Raman scattering SrTiO₃ and KTaO₃. *Phys. Rev.* **174**, 613 (1968).
- Schooley, J. F., Hosler, W. R. & Cohen, M. L. Superconductivity in semiconducting SrTiO₃. *Phys. Rev. Lett.* **12**, 474–475 (1964).
- Thompson, J. R., Boatner, L. A. & Thomson, J. O. Very low-temperature search for superconductivity in semiconducting KTaO₃. *J. Low Temp. Phys.* **47**, 467 (1982).
- Ueno, K. et al. Discovery of superconductivity in KTaO₃ by electrostatic carrier doping. *Nature Nano.* **6**, 408–412 (2011).
- Liu, C. et al. Two-dimensional superconductivity and anisotropic transport at KTaO₃ (111) interfaces. *Science* **371**, 716–721 (2021).
- Chen, Z. et al. Electric field control of superconductivity at the LaAlO₃/KTaO₃ (111) interface. *Science* **372**, 721–724 (2021).
- Reyren, N. et al. Superconducting interfaces between insulating oxides. *Science* **317**, 1196–1199 (2007).
- Caviglia, A. D. et al. Electric field control of the LaAlO₃/SrTiO₃ interface ground state. *Nature* **456**, 624–627 (2008).
- Biscaras, J. et al. Two-dimensional superconducting phase in LaTiO₃/SrTiO₃ heterostructures induced by high-mobility carrier doping. *Phys. Rev. Lett.* **108**, 247004 (2012).
- Chen, Z. et al. Two-dimensional superconductivity at the LaAlO₃/KTaO₃ (110) heterointerface. *Phys. Rev. Lett.* **126**, 026802 (2021).
- Liu, C. et al. Tunable superconductivity at the oxide-insulator/KTaO₃ interface and its origin. Preprint at arXiv:2203.05867 (2022).
- Berezinskii, V. L. Destruction of long-range order in one-dimensional and two-dimensional systems possessing a continuous symmetry group. II. Quantum systems. *Sov. Phys. JETP* **34**, 610 (1972).
- Kosterlitz, J. M. & Thouless, D. J. Ordering, metastability and phase transitions in two-dimensional systems. *J. Phys. C* **6**, 1181 (1973).
- Kosterlitz, J. M. The critical properties of the two-dimensional xy model. *J. Phys. C* **7**, 1046 (1974).
- Venditti, G. et al. Nonlinear I-V characteristics of two-dimensional superconductors: Berezinskii-Kosterlitz-Thouless physics versus inhomogeneity. *Phys. Rev. B* **100**, 064506 (2019).
- Vaz, D. C. et al. Mapping spin-charge conversion to the band structure in a topological oxide two-dimensional electron gas. *Nature Mat.* **18**, 1187–1193 (2019).
- Vicente-Arche, L. M. et al. Metal/SrTiO₃ two-dimensional electron gases for spin-to-charge conversion. *Phys. Rev. Mat.* **5**, 064005 (2021).
- Rödel, T. C. et al. Universal fabrication of 2D electron systems in functional oxides. *Adv. Mater.* **28**, 1976–1980 (2016).
- Vicente-Arche, L. M. et al. Spin-charge interconversion in KTaO₃ 2D electron gases. *Adv. Mater.* **33**, 2102102 (2021).
- Biscaras, J. et al. Limit of the electrostatic doping in two-dimensional electron gases of LaXO₃ (X = Al, Ti)/SrTiO₃. *Sci. Rep.* **4**, 6788 (2014).

22. Jaeger, H. M., Haviland, D. B., Orr, B. G. & Goldman, A. M. Onset of superconductivity in ultrathin granular metal films. *Phys. Rev. B* **40**, 182–196 (1989).
23. Orr, B. G., Jaeger, H. M. & Goldman, A. M. Local superconductivity in ultrathin Sn films. *Phys. Rev. B* **32**, 7586(R) (1985).
24. Singh, G. et al. Effect of disorder on superconductivity and Rashba spin-orbit coupling in LaAlO₃/SrTiO₃ interfaces. *Phys. Rev. B* **96**, 024509 (2017).
25. Tinkham, M. *Introduction to Superconductivity* 2nd edn (Dover Publications, Inc., 2004).
26. Singh, G. et al. Competition between electron pairing and phase coherence in superconducting interfaces. *Nat. Commun.* **9**, 407 (2018).
27. Singh, G. et al. Gap suppression at a Lifshitz transition in a multi-condensate superconductor. *Nature Mat.* **18**, 948–954 (2019).
28. Epstein, K., Goldman, A. M. & Kadin, A. M. Vortex-antivortex pair dissociation in two-dimensional superconductors. *Phys. Rev. Lett.* **47**, 534 (1981).
29. Epstein, K., Goldman, A. M. & Kadin, A. M. Renormalization and the Kosterlitz-Thouless transition in a two-dimensional superconductor. *Phys. Rev. B* **27**, 6691 (1983).
30. Fiory, A. T., Hebard, A. F. & Glaberson, W. I. Superconducting phase transitions in indium/indium-oxide thin-film composites. *Phys. Rev. B* **28**, 5075 (1983).
31. Turneaure, S. J., Lemberger, T. R. & Graybeal, J. M. Effect of thermal phase fluctuations on the superfluid density of two-dimensional superconducting films. *Phys. Rev. Lett.* **84**, 987 (2000).
32. Crane, R. W. et al. Fluctuations, dissipation, and nonuniversal superfluid jumps in two-dimensional superconductors. *Phys. Rev. B* **75**, 094506 (2007).
33. Liu, W., Kim, M., Sambandamurthy, G. & Armitage, N. P. Dynamical study of phase fluctuations and their critical slowing down in amorphous superconducting films. *Phys. Rev. B* **84**, 024511 (2011).
34. Kamlapure, A. et al. Measurement of magnetic penetration depth and superconducting energy gap in very thin epitaxial NbN films. *Appl. Phys. Lett.* **96**, 072509 (2010).
35. Mondal, M. et al. Role of the vortex-core energy on the Berezinskii-Kosterlitz-Thouless transition in thin films of NbN. *Phys. Rev. Lett.* **107**, 217003 (2011).
36. Misra, S., Urban, L., Kim, M., Sambandamurthy, G. & Yazdani, A. Measurements of the magnetic-field-tuned conductivity of disordered two-dimensional Mo₄Ge₅₇ and InOx. Superconducting films: evidence for a universal minimum superfluid response. *Phys. Rev. Lett.* **110**, 037002 (2013).
37. Yong, J., Lemberger, T., Benfatto, L., Ilin, K. & Siegel, M. Robustness of the Berezinskii-Kosterlitz-Thouless transition in ultrathin NbN films near the superconductor-insulator transition. *Phys. Rev. B* **75**, 184505 (2013).
38. Ganguly, R., Chaudhuri, D., Raychaudhuri, P. & Benfatto, L. Slowing down of vortex motion at the Berezinskii-Kosterlitz-Thouless transition in ultrathin NbN films. *Phys. Rev. B* **91**, 054514 (2015).
39. Bareille, C. et al. Two-dimensional electron gas with six-fold symmetry at the (111) surface of KTaO₃. *Sci. Rep.* **4**, 3586 (2014).
40. Bruno, F. Y. et al. Band structure and spin-orbital texture of the (111)-KTaO₃2D electron gas. *Adv. Electron. Mater.* **5**, 1800860 (2019).
41. Manca, N. et al. Bimodal phase diagram of the superfluid density in LaAlO₃/SrTiO₃ revealed by an interfacial waveguide resonator. *Phys. Rev. Lett.* **122**, 036801 (2019).
42. Bert, J. A. et al. Gate-tuned superfluid density at the superconducting LaAlO₃/SrTiO₃ interface. *Phys. Rev. B* **86**, 060503(R) (2012).
43. Benfatto, L., Castellani, C. & Giamarchi, T. in *40 Years of Berezinskii-Kosterlitz-Thouless Theory* (ed. Josè, J. V.) Ch. 5 (World Scientific, 2013).
44. Nelson, D. R. & Kosterlitz, J. M. Universal jump in the superfluid density of two-dimensional superfluids. *Phys. Rev. Lett.* **39**, 1201–1205 (1977).
45. McQueeney, D., Agnolet, G. & Reppy, J. D. Surface superfluidity in dilute ⁴He-³He mixtures. *Phys. Rev. Lett.* **52**, 1325 (1984).
46. Benfatto, L., Castellani, C. & Giamarchi, T. Broadening of the Berezinskii-Kosterlitz-Thouless superconducting transition by inhomogeneity and finite-size effects. *Phys. Rev. B* **80**, 214506 (2009).
47. Mondal, M. et al. Phase fluctuations in a strongly disordered s-wave NbN superconductor close to the metal-insulator transition. *Phys. Rev. Lett.* **106**, 047001 (2011).
48. Maccari, I., Benfatto, L. & Castellani, C. Broadening of the Berezinskii-Kosterlitz-Thouless transition by correlated disorder. *Phys. Rev. B* **96**, 060508 (R) (2017).
49. Ambegaokar, V., Halperin, B. I., Nelson, D. R. & Siggia, E. D. Dynamics of superfluid films. *Phys. Rev. B* **21**, 1806 (1979).
50. Halperin, B. I. & Nelson, D. R. Resistive transition in superconducting films. *J. Low. Temp. Phys.* **36**, 599 (1979).
51. Zhang, G. et al. Spontaneous rotational symmetry breaking in KTaO₃ interface superconductor. Preprint at arXiv:2111.05650v2 (2021).
52. Kirkpatrick, S. Percolation and conduction. *Rev. Mod. Phys.* **45**, 574 (1973).

Acknowledgements

This work was supported by the ANR QUANTOP Project-ANR-19-CE47-0006 grant, by the QuantERA ERA-NET Cofund in Quantum Technologies (Grant Agreement N. 731473) implemented within the European Union's Horizon 2020 Program (QUANTOX), by EU under project MORE-TEM ERC-SYN (grant agreement No 951215) and by Sapienza University of Rome, through the projects Ateneo 2019 (Grant No. RM11916B56802AFE) and Ateneo 2020 (Grant No. RM120172A8CC7CC7), and by the Italian MIUR through the Project No. PRIN 2017Z8TS5B.

Author contributions

N.B. and M.B. proposed and supervised the study. S.M. and H. W. prepared the samples and performed XPS experiments and their analysis. A.G. performed the STEM and EELS analysis. G.C.M., G.S., and S.M. performed the dc and microwave transport experiments and analysed the data with input from M.B., J.L., and N.B. L.B. conducted the BKT analysis of microwave data. N.B., M.B., and L.B. wrote the manuscript with input from all authors. All authors discussed the results and contributed to their interpretation.

Competing interests

The authors declare no competing interests.

Additional information

Correspondence and requests for materials should be addressed to N. Bergeal.

Peer review information *Nature Communications* thanks the anonymous reviewer(s) for their contribution to the peer review of this work.

Reprints and permission information is available at <http://www.nature.com/reprints>

Publisher's note Springer Nature remains neutral with regard to jurisdictional claims in published maps and institutional affiliations.

Open Access This article is licensed under a Creative Commons Attribution 4.0 International License, which permits use, sharing, adaptation, distribution and reproduction in any medium or format, as long as you give appropriate credit to the original author(s) and the source, provide a link to the Creative Commons license, and indicate if changes were made. The images or other third party material in this article are included in the article's Creative Commons license, unless indicated otherwise in a credit line to the material. If material is not included in the article's Creative Commons license and your intended use is not permitted by statutory regulation or exceeds the permitted use, you will need to obtain permission directly from the copyright holder. To view a copy of this license, visit <http://creativecommons.org/licenses/by/4.0/>.

© The Author(s) 2022